Building Practical Descriptors for Defect Engineering of Electrocatalytic Materials

Raphaël Chattot, Pierre Bordet, Isaac Martens, Jakub Drnec, Laetitia Dubau, Frédéric Maillard

Viewpoint

Building Practical Descriptors for Defect Engineering of Electrocatalytic Materials

Raphaël Chattot, Pierre Bordet, Isaac Martens, Jakub Drnec, Laetitia Dubau, and Frédéric Maillard

ACS Catal., **Just Accepted Manuscript** • DOI: 10.1021/acscatal.0c02144 • Publication Date (Web): 13 Jul 2020

Building Practical Descriptors for Defect Engineering of Electrocatalytic Materials

*Raphaël Chattot [†, ‡, *], Pierre Bordet [⊥], Isaac Martens [‡], Jakub Drnec [‡], Laetitia Dubau [†] and Frédéric Maillard [†, *]*

† Univ. Grenoble Alpes, Univ. Savoie Mont Blanc, CNRS, Grenoble INP, LEPMI, 38000 Grenoble, France

‡ European Synchrotron Radiation Facility, ID 31 Beamline, BP 220, F-38043 Grenoble, France

⊥ Univ. Grenoble Alpes, CNRS, Institut Néel, F-38000 Grenoble, France

KEYWORDS: Electrocatalysis; Oxygen Reduction Reaction; Defect Engineering; Structural Disorder; Nanomaterials.

TEXT

Defect engineering has recently gained considerable interest in electrocatalysis by extending the portfolio of materials design strategies toward more efficient and sustainable nanocatalysts [1]. This approach is highly versatile as the term ‘defect’ in crystallography refers to any interruption of the regular pattern defining a perfect crystal. As such, point defects (atomic vacancies, interstitial atoms, antisite defects) line defects (dislocations, disclinations), planar defects (grain boundaries, stacking faults, twinning, steps) or bulk defects (voids, pores, cracks) are a non-exhaustive list of structural parameters to be possibly tailored to meet a catalytic material functional specifications. In contrast to former approaches in electrocatalysis, within the defects engineering strategies, electrocatalytic properties are tuned locally not globally. Indeed, defects produce (simultaneous) local changes in key structural parameters relative to catalytic performance, such as site coordination, strain or chemical composition.

Historically, density functional theory (DFT) calculations, molecular dynamics and kinetic Monte Carlo simulations have been extensively used to connect the catalytic

site local environment to its catalytic properties from computational screening over the trial-and-error approach [2]. These methods rely on the determination of catalytic site electronic structure that can be further bridged to the catalytic performance through the adsorption strength of reaction intermediates. Especially, for a given reaction mechanism, focusing on the 'limiting' reaction step(s) in the frame of Sabatier principle represents a remarkably powerful and efficient route toward the reduction of numerous system variables to few 'key' reactivity descriptors [3]. In case of the sluggish oxygen reduction reaction (ORR) on Pt, which restricts the development of proton exchange membrane fuel cells (PEMFC), the existence of so-called scaling relations between the *O, *OH and *OOH intermediates adsorption strengths allows focusing on a single of these adsorbate. In that frame, calculations predict the optimal ORR rate is obtained by decreasing the adsorption energy of *O (or by extension *OH and *OOH) by ~0.2 eV (or ~0.1 eV) compared to Pt(111) [4]. The pivotal correlation between adsorption trends of reaction intermediates and catalytic sites electronic structure is described by the *d*- band model introduced by Hammer and Nørskov [5,6]. Since from this principle, the catalytic properties of a site can be determined completely by its electronic

structure, descriptors of the *d*-band ultimately become (electronic) reactivity descriptors.

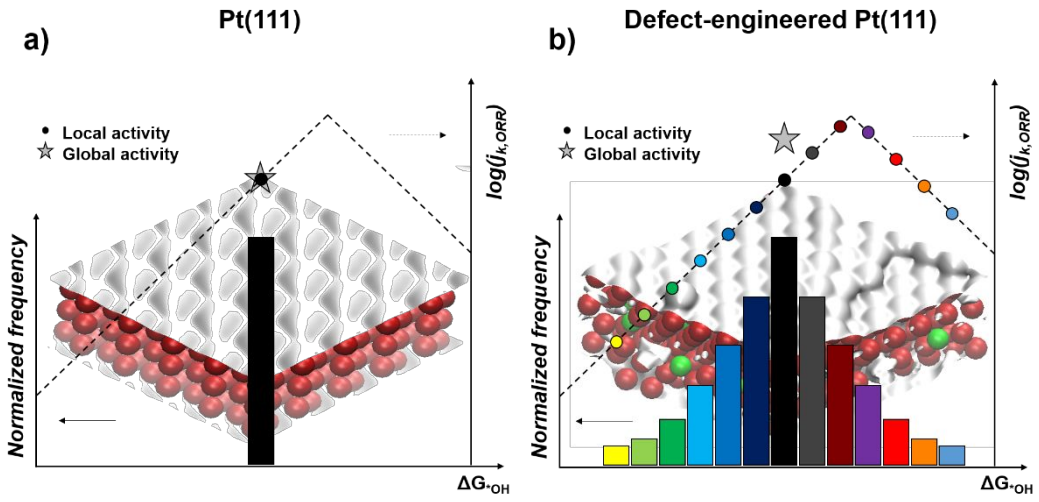

Figure 1. The defect engineering approach. Schematic representation principle of the narrow *vs.* near-continuous broad distributions of catalytic sites configurations and electrocatalytic performance for (a) ordered, model *vs.* (b) defective Pt(111) surfaces.

Fig. 1a illustrates how the *d*-band theory applies to a model Pt(111) surface, where all sites are equivalent (uniform coordination, interatomic distances and chemical environment). The surface thus features a Dirac type *OH adsorption free energy (ΔG_{*OH}) distribution, centered on the value expected for a single Pt(111) site, and its global activity (star symbol) can thus be virtually described by that of a single catalytic site (circle symbol). In contrast, Fig. 1b displays the situation when structural disorder is present at the surface (defect-engineered Pt(111) surface). Here, the coexistence

of sites with various local environments results in a broad, near-continuous distribution of chemisorption properties [7,8]. Supposing the scaling relations still hold, this implies that the global catalytic activity of the surface can no longer be described by that of a single site, but rather as the average catalytic activity of each site. Consequently, whereas the ORR activity of flat Pt(111) is limited by the overall too strong affinity with *OH species (left branch of the volcano), a minority of catalytic sites with close-to-optimal structural configuration, but exponential contribution to the global activity (Butler-Volmer kinetics), ensures enhanced ORR activity for the defect-engineered Pt(111) surface.

However, structure-sensitive, electronic descriptors alone (such as the *d*-band center, ε_d) do not provide any clear-cut reverse structural information about the catalytic site local environment that could guide material design. Also, even if computational methods from model structures can correlate a fine local atomic motif and electronic properties (see coordination-based descriptors such as $\overline{\mathrm{CN}}$ [9], CN^{α} [10] or $\overline{\mathrm{CN}}^{\mathrm{sd}}$ [11]), ensuring the successful implementation of such fine atomic motif onto practical nanocatalysts surface remains extremely difficult. That is because (i) it requires an

atomic scale control of the surface structure design (other than atomically flat) and (ii) characterization techniques are limited in describing such fine structural atomic motifs on 'real-life' nanocatalysts. This apparent dichotomy between extremely fine theoretical insights on well-defined systems and the extreme complexity of poorly defined practical systems is at the heart of the defect engineering current challenge. Whereas the uniformity of the catalytic sites was a convenient pillar of surface science, here each surface atom has its own configuration and should be considered individually (**Fig. 1**). In that frame, practical descriptors able to bridge surface heterogeneous structure and catalytic performance experimentally are of primary importance.

This viewpoint article intends to comment on the establishment of practical descriptors able to guide the defect engineering of practical nanocatalysts. We first discuss the case of the local strain, and especially how an explicit bulk physical parameter can be turned to a surface structural descriptor: the surface distortion (SD). Then, we show how cyclic voltammetry experiments analyzed in light of SD can reveal electrochemical adsorption fingerprint of structural disorder, thus providing a versatile method to

shortcut in-depth structural characterization. Importantly, we emphasize that, because structural or adsorption properties are averaged over the whole catalyst (*i.e.* the spatial resolution is lost), such descriptors do not reveal the nature of the active site but mostly provide statistical insights on their emergence from disorder. Consequently, we finally discuss the opportunities offered by emerging analytical techniques we anticipate will advance our understanding of defect characterization towards identification of electrocatalytically active and stable motifs. Whereas Pt-based catalysts for PEM fuel cell served as discovery platform of the presented methods, all results (except the cyclic voltammetry techniques) apply to other types of nanocatalysts.

1. Physical and electrochemical assessments of local strain to describe surface disorder

Microstrain line broadening in powder X-ray diffraction

Many phenomena synergistically contribute to the diffractograms profile observed in powder X-ray diffraction (PXRD) experiments. As PXRD (especially from laboratory sources) has become a routine technique in numerous fields of research, simple analytical softwares have been developed to extract sample structural information from PXRD data. However, extracting reliable information related to the quantification of structural disorder requires a rigorous methodology to minimize the impact of errors related to both experimental and interpretation artifacts. Numerous analytical approaches such as Williamson-Hall method, Warren-Averbach method, Fourier method or full profile refinement (Rietveld, Le Bail) methods can be used to investigate the micro-structure of a powder sample from PXRD data. In case of nanocrystals with sizes <10 nm, extensive peak broadening and overlap makes the methods based on the analysis of few individual reflections inaccurate and full profile refinement technique of PXRD patterns extending over a large *Q*-range are preferred (see **Fig.**

2a). This reason, together with the versatility offered by the full profile refinement methods in terms of peak shape description and possible anisotropy consideration, make the Rietveld method [12] highly attractive, despite its complexity due to the large number of control parameters.

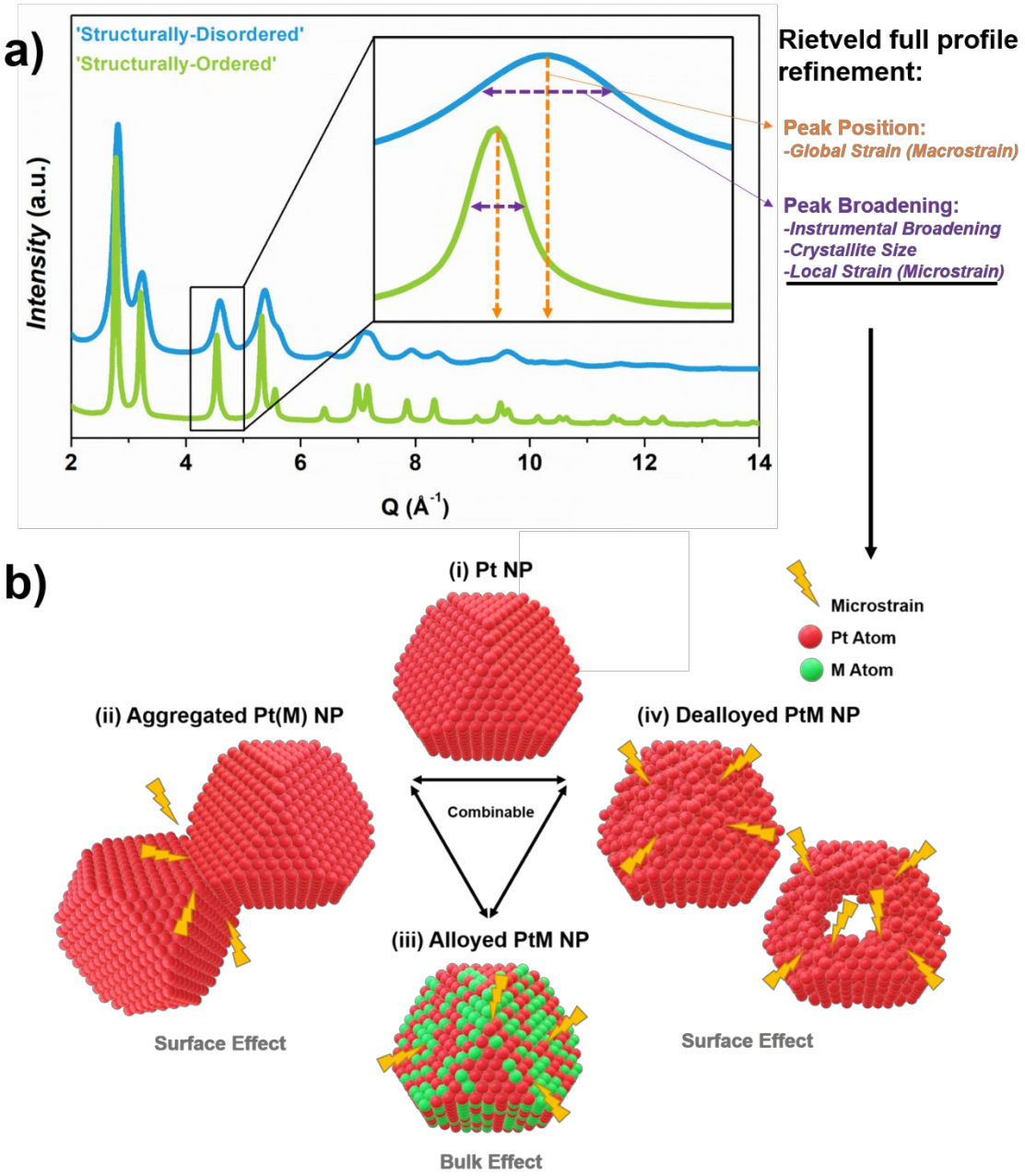

Figure 2. Powder X-ray diffraction (PXRD) patterns broadening and sources of microstrain in PtM nanoparticles (M being an early or late transition metal element). (a) Typical experimental PXRD patterns measured at the high energy ID31 beamline of the European Synchrotron Radiation facility on structurally disordered and structurally ordered catalysts (here hollow PtNi/C and cube Pt/C nanoparticles, respectively) plotted as a function of the momentum transfer *Q*. (b) Possible sources of microstrain in PtM nanocatalysts (grain boundaries, inhomogeneous alloying or (electro)chemical surface dealloying). The insert in (a) shows the influence of macrostrain, instrumental contribution and microstrain on the position and the broadening of the PXRD reflections. Adapted from Ref [13]. Copyright 2018 Springer Nature.

It is generally admitted that the Bragg peak profile (shape and width) can be described as the convolution of three contributions: (i) the incident X-ray beam monochromaticity, (ii) the instrument optics (slit gaps and positions, detector pixel size *etc.*) and (iii) sample-related broadening effects. The latter is the consequence of two microstructural properties of the sample investigated, namely the finite size of the coherent domains (or grain size), and the presence of microstrain (or local strain, the parameter of interest here), which reflects the local variations of inter interplanar distances caused by some sort of stress (disorder, stacking fault, twins, grain boundaries, inhomogeneous alloying *etc.*, see **Fig. 2b**). As described in the Supporting Information, the Rietveld method can disentangle microstrain broadening from other contributions, thus providing a physical parameter that is representative of local strain originating from structural disorder.

Rietveld refinement of powder X-ray diffractograms becomes limited when the nanoparticle size is substantially smaller than the beam coherence length, (*i.e.* typically a few nanometers [14]) and a periodic crystal-type description of the atomic arrangement breaks down, so as does the Bragg's law. In such case, Pair Distribution

Function (PDF) analysis of total scattering data can provide quantitative information on the structural and microstructural properties of nanocatalysts [15]. Experimentally, the PDF is obtained from a PXRD pattern by realizing the Fourier transform as:

$$G(r) = 4\pi r[\rho(r) - \rho_0] = \frac{2}{\pi}\int_{Q_{min}}^{Q_{max}} Q[S(Q) - 1]\sin(Qr)dQ \quad (1)$$

Where $\rho(r)$ is the microscopic pair density and $Q = 4\pi.\sin(\theta)/\lambda$. $S(Q)$ is the total structure function, *i.e.* the normalized coherent scattered intensity obtained from the PXRD pattern after subtraction of the environment and inelastic/incoherent scattering and normalization. It is worth noting that the whole diffraction pattern is used to obtain $G(r)$, not only the Bragg peak intensities as for Rietveld refinement. Therefore, the effects of disorder, defects, etc. which contribute to the pattern through diffuse scattering outside of the Bragg peaks, will also be included in $G(r)$. The PDF yields the probability of finding a pair of atoms separated by a distance r. It will oscillate in a way that is characteristic of a given structure, about the average pair density that would result from a completely unordered atomic arrangement. Thus, it can be calculated

from a structural model describing the distribution of atoms in a sample. The calculated PDF can be fitted to the observed one, as in a 'direct space Rietveld refinement'. The fit is carried out in a given interatomic distance range, yielding accurate structural parameters relative to this range. Comparing refinements for very small or longer distances allows revealing the presence of local structural distortions with respect to an average long-range atomic arrangement. In addition, the PDF signal vanishes for distances longer than the structural coherence length (or domain size), which provides a simple way to determine the average nanoparticle size in a sample. On the other hand, the effect of microstrain will be to broaden the distribution of interatomic distances about their average values, which will result in a broadening of the corresponding peaks of the PDF. The PDF is thus sensitive to microstrain, however its effect is combined to thermal displacement and instrumental broadening, from which it is difficult to extract. The PDF can also be used with Reverse Monte Carlo minimization of large atomic assemblies, which allows a statistical description of samples from liquids and amorphous to crystalline nanoparticles [16].

From bulk microstrain to surface distortion

The main reason to correct microstrain values is related to the definition of microstrain itself, which links a local variation of the interplanar distance *d* between *d*-Δd and *d*+ Δd according to:

$$\varepsilon = \frac{\Delta d}{d} \quad (2)$$

In practice, there is a distribution of $\Delta d/d$ within and across the coherent domains. The refined ε value thus corresponds to the root mean square $< \varepsilon >$, averaged over all crystallites in the sample. Consequently, microstrain is a *global* and *relative* estimation of structural disorder, since the even perfectly ordered domains (Δd = 0) also contribute to the average value. To build a consistent structure-activity relationship in heterogeneous catalysis, a *surface-specific* and *quantitative* structural descriptor is needed. To fulfill these requirements, two complementary 'corrections' of the as-measured microstrain values were proposed [13,17]. These corrections derive from experimental (electron microscopy observations [18–23]) and theoretical studies [8,13,24],

which suggest that microstrain can be decomposed into two main and independent contributions:

- The surface microstrain mostly associated with the presence of grain boundaries and/or arising from dealloying. Despite surface bound, such microstrain values are relative and need to be corrected from the crystallite size;
- The microstrain of the whole crystallite volume (mostly arising from heterogeneous alloying and hereafter referred as 'chemical disorder' in what follows). Such microstrain is not representative of the surface and must be estimated and subtracted.

As detailed in the Supporting Information, for PtM bimetallic catalysts, these hypotheses allow to decompose the measured microstrain as a sum of bulk chemical disorder (f(%M), estimated experimentally or from DFT calculations) and surface defectiveness (SD), weighted by the surface-to-volume ratio (D, calculated using Montejano-Carrizales *et al.*'s model [25]):

$$\text{Microstrain} = f(\%M) + D * \text{SD} \quad (3)$$

Fig. 3 shows how the SD descriptor can be used to unveil the 'operating mode' of a library of Pt and PtNi nanocatalysts. The ORR specific activity-SD plot in Fig. 3.k indicates that enhanced ORR activity arises from two distinct approaches:

- The global surface tuning approach (null and low SD values), derived from DFT calculations and single crystal studies, which aims at enhancing the ORR rate by synthetically tailoring and maximizing the density of catalytic sites that weakly chemisorb the ORR intermediates (in this category, octahedral PtNi nanoparticles feature the highest ORR activity),
- The local surface tuning, or defect-engineering approach (high SD values), in which the ORR rate is controlled by the fraction of catalytic sites with close-to-optimal affinity to the ORR intermediates.

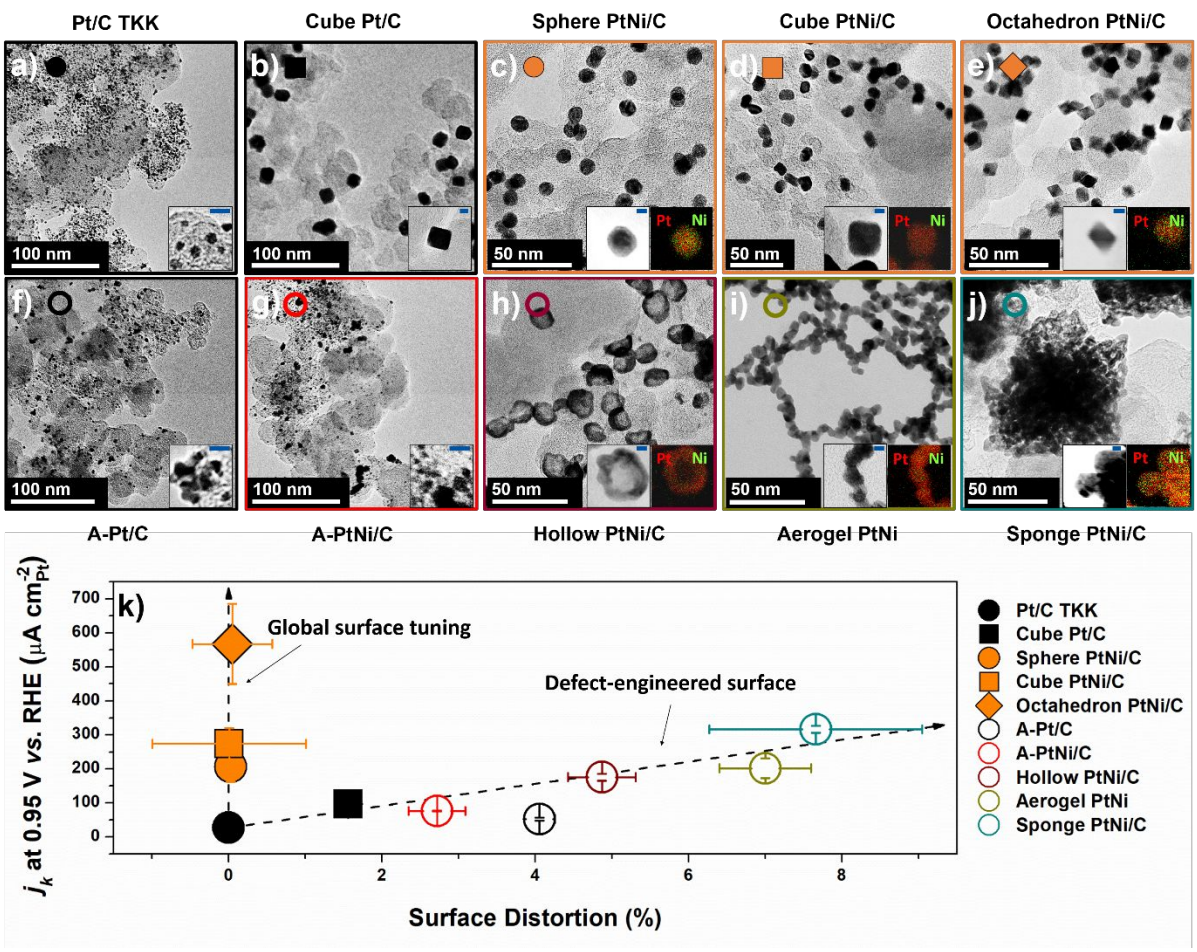

Figure 3. Using the SD descriptor to unveil the 'operating mode' of a variety of ORR nanocatalysts. (a-j) TEM images of the various nanostructures investigated. The inserts show higher magnification TEM or STEM/X-EDS elemental maps. (k) ORR activity measured at 0.95 V *vs.* RHE plotted as a function of the SD descriptor. The activity-SD plot quantitatively confirms that high ORR activity can be reached through the two approaches presented in Fig. 1. Panels (a-j) are reprinted with permission from Ref [26]. Copyright 2020 American Chemical Society. Panel (k) is adapted with permission from Ref [13]. Copyright 2018 Springer Nature.

It is noteworthy that, as SD values are derived from microstrain values, they are only sensitive to the local strain caused by defects, and do not take into account other ORR-relevant fundamental parameters such as the average lattice contraction (global strain), the near surface chemical composition or the site coordination (that is why

multiple ORR activities can be found at low SD values). However, the fact that the ORR activities increase almost linearly with the SD values (**Fig. 3.k**) is clear evidence that, (i) similar to the 'classical' strain and ligand effects, surface disorder plays a key role in ORR electrocatalysis and (ii) local strain alone is one, if not the most, influential facets of disorder on catalytic performance.

Quantifying surface distortion from cyclic voltammetry

As discussed previously, the fundamental and direct consequence of structural disorder is the emergence of a wide variety of catalytic site configurations on a given electrocatalytic surface (**Fig. 1b**). DFT calculations by Le Bacq *et al.* [8,13] have revealed a ± 1 eV distribution width in *OH binding energy on structurally disordered Pt surfaces. Whereas a fraction of these catalytic sites is statistically close to the optimal configuration for a given catalytic reaction (~0.1 eV weaker chemisorption of *OH in the case of the ORR), another fraction is in the optimal configuration for a different reaction. Indeed, highly aggregated/polycristalline nanocatalysts have demonstrated desirable catalytic performances for a wide range of electrochemical reactions including the ORR [17,27–35], the CO electrooxidation [17,36], the methanol or ethanol

electrooxidation [8,37–39], the hydrogen evolution reaction (HER) and the OER [40–43]. Consequently, surface disorder and catalytic polyvalence must be somehow linked, and similar SD-activity plot should be found for almost any reaction, at least involving *OH species.

In that frame, CO_{ads} stripping (here referred to COOR) can be chosen as a complementary reaction to the ORR to investigate surface catalytic polyvalence because the prerequisite for optimal COOR are different regarding *OH adsorption strength (increased *OH binding by ~0.4 eV relative to Pt(111) according to Calle-Vallejo *et al.*) [44]. Simultaneous improvement in ORR and COOR specific activity should consequently evidence catalytic polyvalence, and thus surface defectiveness. The COOR activity (or CO tolerance) of a Pt-based nanocatalyst can be quantified by the average CO_{ads} oxidation potential (μ_1^{CO}, or the first moment of the potential weight in the CO_{ads} stripping voltammograms, see details in Ref [17] and examples in **Fig. 4a**).

As shown in **Fig. 4b**, a drawback of using complementary reactions to probe surface catalytic polyvalence is that it is not generally applicable. If structural disorder must induce catalytic polyvalence (μ_1^{CO} generally decreases with increasing SD), the inverse

is not necessarily true. Indeed, the COOR overpotential is not strictly governed only by *OH adsorption strength, but by an appropriate balance between the formation of *OH species and their combination with diffusing [45] *CO species (Langmuir-Hinshelwood mechanism). In practice, not only structural disorder but also crystallite size, surface chemical composition and site coordination influence the *CO binding energy, and thus the μ_1^{CO} values. A very good example of this was provided by Stamenkovic *et al.* [46], who reported simultaneous negative shift of the CO_{ads} stripping profile and tremendous ORR activity for the $Pt_3Ni(111)$-skin surface, in agreement with results from shape-controlled nanoparticles displayed in **Fig. 5b**, especially regarding PtNi octahedra. A method relying only on *OH bond strength is consequently needed.

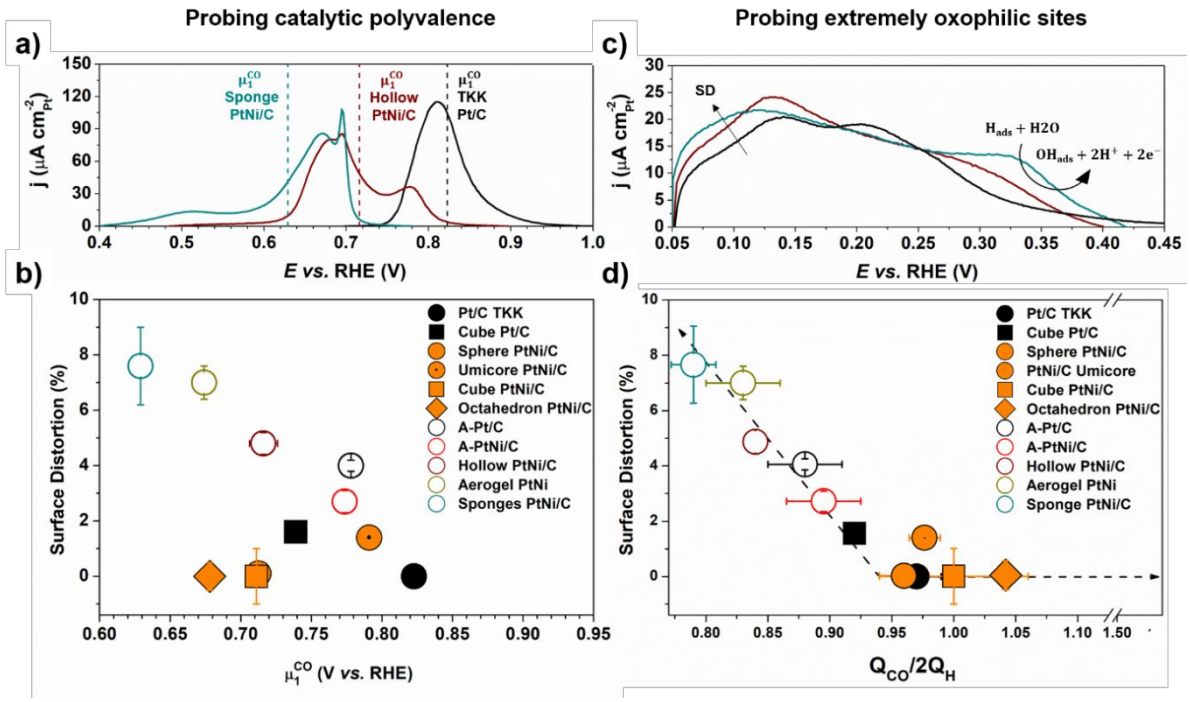

Figure 4. Probing catalytic sites diversity and oxophilicity. (a) Background-subtracted CO_{ads} stripping voltammograms recorded on Pt and PtNi nanomaterials featuring increasing SD values and their associated average potential μ_1^{CO} (dashed lines), (b) SD plotted as a function of the COOR activity (μ_1^{CO}) for a wide range of PtNi materials with different shape, size or Ni content. (c) background-subtracted H_{ads} desorption curves (so called-H_{UPD} region) of materials featuring increasing SD values pointing an extra electrochemical process at high potential ascribed to *H displacement by *OH on extremely oxophilic sites, and (d) SD plotted as a function of the ratio $Q_{CO}/2Q_H$ for a wide range of PtNi materials with different shape, size or Ni content. In (b), the numbers displayed close to the experimental points are the SD values associated to these catalysts. In both (a) and (c), the curves are normalized by the Pt surface area measured by CO_{ads} stripping. Panel (d) is adapted from permission of ref [26]. Copyright 2020 American Chemical Society.

It is deduced from the extremely low COOR onset potential observed in case of highly defective Sponge PtNi/C in **Fig. 4a** (~0.4 V *vs*. RHE) that *OH species are adsorbed on the surface at such low electrode potentials. The idea of concomitant adsorption of *OH and under-potentially deposited hydrogen (H_{UPD}) has been discussed many years

ago by Marichev *et al.* [47], Van Der Niet *et al.* [48], and more recently by Janik *et al.* [49]. The results of infrared spectroscopy (IRAS) [50] and CO displacement measurements [51] on extended surfaces, as well as DFT calculations, have suggested that *H species adsorbed on extremely oxophilic sites can be displaced by *OH species, following an electrochemical reaction of the type:

$$^{*}\mathrm{H} + \mathrm{H_2O} \leftrightarrow {}^{*}\mathrm{OH} + 2\mathrm{H}^{+} + 2\mathrm{e}^{-} \quad (4)$$

The displacement process described by **Eq. 4** creates an extra charge compared to the charge required just to desorb under-potentially deposited H atoms (Q_H). Consequently, an increase in Q_H compared to the CO_{ads} stripping charge (Q_{CO}), as experimentally observed in **Fig. 4c**, supports the presence of highly oxophilic sites on Pt-based surfaces [26].

Most importantly, as displayed in **Fig. 4d**, contrary to μ_1^{CO}, the $Q_{CO}/2Q_H$ ratio measured on a wide range of nanocatalysts decreases almost linearly only with strictly positive values of SD, independently from other structural and chemical parameters. This suggests that such highly oxophilic sites are possibly generated only from structural disorder, *i.e.* there are not the 'simple' undercoordinated sites found at nanoparticles

surface edges, steps or kinks (otherwise, low $Q_{CO}/2Q_H$ ratio would be systematically found on nanocatalysts). In other words, the $Q_{CO}/2Q_H$ ratio quantitatively probes the fraction of highly oxophilic sites, which catalyze the process described by **Eq. 4**. Because such extreme *OH adsorption energies are more likely reached *via* the broadening of the *OH adsorption energies distribution than its simple uniform shift, the ratio indirectly quantifies the structural disorder responsible for this broadening. This hypothesis is supported by the SD-$Q_{CO}/2Q_H$ plot in **Fig. 4d** and the ORR activity-$Q_{CO}/2Q_H$ plot in **Fig. S2** of the Supporting Information, which show that, counter-intuitively, the ORR activity increases with increasing fraction of highly oxophilic sites. This result is of primary importance since the $Q_{CO}/2Q_H$ ratio can thus be used to estimate the degree of surface defectiveness of a given catalyst, just as the synchrotron X-ray based SD descriptor does, yet in a much more facile and accessible way. Besides, this method is by definition truly surface sensitive, likely incorporating the effects of coordination and/or chemical composition variations as well as local strain. The method can also be employed *operando*, *i.e.* in a PEMFC device [26]. Nevertheless, although these descriptors (SD and/or $Q_{CO}/2Q_H$) have a great advantage to provide insights on the statistical existence of active atomic motifs over

the whole catalyst surface, the exact structure of these motifs and their location on the surface remain largely unknown.

2. Perspectives toward the identification of the active structural motifs

In the previous section, we showed how the local strain averaged over the whole catalyst surface could serve as a powerful structural descriptor to rationalize the unique electrochemical behaviour of practical disordered surfaces. The SD descriptor, in addition to the $Q_{CO}/2Q_H$ ratio, suggests that increasing surface disorder promotes the emergence of only a fraction of active catalytic sites, in detriment of another fraction. Further insights on the nature of these active sites (such as their location, structural environment or which kind of defect generates them) would certainly guide the optimization of defective nanocatalysts. In the following section, we review several emerging analytical techniques that we believe will play a key role in that purpose.

Electron microscopy tomography

Recent advances in transmission electron microscopy (TEM) methodology regarding spherical and chromatic aberration correction, improvements of cameras, electron guns energy resolution and processing algorithms [52] now allow the imaging and/or 3D

reconstruction of nanoparticles at the atomic scale. For example, using aberration corrected scanning transmission electron microscopy (AC-STEM) operated in annular dark field mode (STEM-ADF) tomography coupled with a generalized Fourier iterative reconstruction (GENFIRE) algorithm, Yang *et al.* [22] determined the coordinates of each atom composing a face-centered tetragonal (L_{10}) PtFe nanoparticle (**Fig. 5a**). Atomic coordinate determination represents the ultimate structural characterization one can expect, and the results showed that a nominally ordered particle was in fact composed of 8 individual grains, each featuring a different phase, including ordered $L1_0$ and $L2_0$ or disordered face-centered cubic (*fcc*) phases. Each surface atom coordination, local displacement compared to the perfect crystal structure and local chemical environment can be determined from such measurements. Similarly, an increasing number of studies [18–23] have successfully mapped the distribution of strain in extended surfaces or mono- and bi-metallic nanoparticles. Using high-resolution scanning transmission electron microscopy (HRSTEM), Nilsson *et al.* [21] have reported that the bulk of Pt nanoparticles supported on alumina or ceria is (“rather”, as employed by the authors) deformation-free. Interestingly, local strain was systematically detected close to twin boundaries, at high surface curvature (convex

edge sites or concavities) and at the nanoparticle-support interface (see in **Fig. 5b**), in agreement with other TEM studies [22,23,53,54]. In addition, the 'true' surface strain distribution was directly deduced from the data, which constitutes an improvement compared to SD that requires numerous hypotheses. This direct strain-defect type correlation is precious for the defect engineering approach. It also evidences that coordination and strain are strongly linked.

However, these measurements are extremely resource demanding and are usually limited to a limited number of nanoparticles, which are supposed to be representative of the whole catalyst. In addition, identical-location-aberration-corrected scanning STEM (IL-AC-STEM) measurements [23] evidenced that atomic coordinates measured under TEM vacuum conditions change upon exposure to a PEMFC-relevant electrochemical environment, which compromises the straightforward establishment of valid structure-activity relationships from *ex situ* TEM imaging. Moreover, while environmental *in situ* TEM methods are also progressing [52], the dramatic impact of electron-irradiation on nanomaterials structure and chemistry in liquid cells is a major issue that cannot be neglected [55].

Atom probe tomography (APT)

Kelly *et al*. [56] have stated that « *The ideal microscope would reveal the position and identity of all atoms in a specimen for as far as the user wishes to see*» and have added that "*atom probes approach this ideal*". APT is based on the evaporation of a specimen atom by atom, layer by layer, from its surface by field effect; the ions being further projected onto a position sensitive detector. The detector allows the simultaneous determination of position and the element evaporated. The position and the order of arrival of the ion impact on the detector allows one to reconstruct the original position of the atoms on the initial tip and the time of flight of the ions contains their elemental identity via the mass to charge ratio. The sample must be in the form of a very sharp or a needle-shape tip. This is critical because the atoms are progressively removed from the tip allowing the reconstruction of a 3D image of the sample at the atomic scale. In relation with the concerns of the present paper, the combination of highly sensitive composition measurement and three-dimensional microstructural characterization represents a useful tool for the characterization of

structural defects. Indeed, APT has the unique capacity to study chemical segregation to crystalline defects such as dislocations, stacking faults and grain boundaries [57].

Recently, APT has met fundamental electrocatalysis. The oxidation/reduction behavior of Pt-based alloys has been studied at different temperatures to show preferential segregation effect of one metal. Oxidation of PtRhRu alloy was dynamically been monitored, and it was shown that oxidation is initiated at grain boundaries and propagates to form a Ru and Rh-rich oxide [58]. APT also revealed the interplay between surface structure/composition, activity for oxygen evolution reaction (OER) and stability of electrochemical Ir oxide [59]. At first stage of metallic Ir oxidation by anodic polarization, the high OER activity was rationalized by the formation of non-stoichiometric Ir oxide (IrO_x with x <2) clusters composed of a very limited number of atoms (only few tens) predominantly located at grain boundaries. This structure gradually evolves towards more stable but less active IrO_2. By combining isotope labelling and APT, the same group has demonstrated that oxygen from the hydrated Ir oxide participates in the formation of molecular oxygen, and that this mechanism accelerates Ir dissolution [59]. Lastly, spatially resolved elemental compositions

achieved by APT have also demonstrated surface compositional changes of NiP catalysts used to electrocatalyze the OER upon ageing in alkaline medium. The APT results provided evidence of the complete depletion of P along with the presence of amorphous and resistive NiO at the near-surface layers of the catalyst, and these results were used to rationalize the OER activity decay [60].

Nevertheless, APT sample preparation remains an issue to envision the use of this technique in the (electro)catalysis field. The specific geometry of the APT tip (in the form of a needle) with an end-tip radius of 30−100 nm is hardly compatible with powder samples such as supported or even unsupported nanoparticles [61]. Similarly, analysis of porous materials usually designed by dealloying processes requires a specific preparation. Pores and voids have to be previously filled to avoid overlapping ion trajectories and distorted reconstructions induced by porosity [62]. Nevertheless, these recent results show that APT is a growing analytical tool in (electro)catalysis and its emergence provides hope for detailed characterization of the topmost atomic surface layers of nanostructured electrocatalysts, keeping in mind that APT overcomes the main limitations of regular TEM. For example, Tedsree *et al.* [63] successfully used APT

to reveal the internal structure of an Ag@Pd core@shell nanoparticle (Fig. 5c), where the close proximity of Ag and Pd elements in the periodic table makes the imaging contrast extremely challenging in TEM.

Advanced (coherent) X-ray methods

Beyond the averaged microstrain values extracted from PXRD, Bragg coherent diffraction imaging (BCDI) is an emerging technique designed specifically for resolving the 3D strain field inside individual nanocrystals using nanofocused X-rays [64] (see **Fig. 5d**). Strain fields inside a nanocrystal create phase shifts in the diffracted beam, producing an interference pattern at the detector. A single 3D rocking curve coherent diffraction pattern can recover 3D images of the electron density and strain inside Pt nanoparticles. Complete datasets can be acquired on the order of minutes per nanocrystal [65]. Strain maps of single nanocrystals allow the structural influence of individual crystal defects to be resolved. The strain field present at the surface of the particle can be quantitatively determined, and different types of strain-inducing defect structures can be visualized (*e.g.* vacancies from alloy leaching vs dislocation loops) [66].

The strain and real space resolutions of BCDI have benefited from ongoing improvements in synchrotron brightness and coherent flux, and now approach those of electron microscopy. The most significant advantage of X-ray based techniques is that they can be performed *in situ* [67,68] with much less beam damage artefacts, and easier electrochemical control compared with TEM methods. The extremely small size of commercial fuel cell Pt catalyst particles (<5 nm) remains, however, below the present spatial resolution limit of BCDI, but shape-controlled model systems and other electrocatalysts are already within reach [69]. The phase sensitivity and strain resolution in BCDI vastly exceeds the real-space electron density resolution of the nanocrystal. More specifically, the presence of point defects can be detected, even when they cannot be atomically resolved, because the locally induced strain field propagates several unit cells away. The increased coherence of X-ray (nano)beams at 4th generation synchrotron sources, such as the Extremely Brilliant Source (EBS) at the European Synchrotron Radiation Facility (ESRF) are expectedly to rapidly advance the ease and applicability of BCDI for *in situ* electrocatalyst strain imaging at the single particle level, under the environment of a PEMFC device.

Complementarily, if one of the major advantages of high energy X-ray based techniques over other methods is their ability to probe practical catalysts *in situ* or even *operando*, the coherent diffraction imaging principles can be also applied to 'revisit' model surfaces. The advantage over experiments on practical nanoparticle systems is that specific defects can be introduced on single crystal surfaces in a well-controlled manner, using techniques such as ion irradiation [70], cathodic atomization[71], and plasma or laser etching [72]. The structure of such model defect engineered surfaces can be resolved *in situ* from surface X-ray diffraction [73] and electrochemical scanning tunneling microscopy (EC-STM) [74,75]. Coherent X-ray diffraction can also be used to reconstruct the local strain fields on extended surfaces. Although experimental protocols and X-ray methodology still require further development, the first steps in this direction have already been taken [76,77].

One of the ultimate goals of nanofocused X-ray beam techniques is to study nanostructured materials *in situ* and *operando* conditions utilizing the X-ray equivalent of a TEM. The main advantage of direct, real space nanofocused beams over reciprocal space imaging techniques is the ease of use and significantly simpler data

analysis, due to the lack of the diffraction phase problem. Currently, dedicated Dark-field hard X-ray microscopy (DFXRM) instruments are being developed at ESRF [78]. The first imaging results are encouraging, but the instrument still lacks the necessary resolution to study catalyst particles in nanometre range. The spatial resolution ultimately depends on the quality of the imaging lens, which is the current bottleneck. However, recent developments in multilayer Laue lenses give hope that this obstacle will be soon surpassed and imaging at the few-nanometre scale can be achieved in the near future [79].

Electrochemical scanning tunneling microscopy noise measurements

Whereas the various methods described above shed light on the complex local structure of disordered surfaces, identification of the electrocatalytically active sites/motifs is pivotal to the further development of the defect-engineering approach. In that frame, it is worth pointing electrochemical scanning tunneling microscopy noise measurements (n-ECSTM) first introduced by Pfisterer *et al*. in 2017 [80]. This technique is based on the energy barrier difference for electrons tunneling from a sample to a STM tip in aqueous electrolyte. The tunneling barrier is sensitive to all the molecules

present along the electrons' path, such as those adsorbed on the electrocatalytic surface [81] and those diffusing to/from the electrochemical double layer [82,83]. Local modifications of the tunneling barrier in turn allow identification of the most active sites for a given reaction (**Fig. 5e**). The n-ECSTM technique revealed that Pt(111) terraces best electrocatalyze the ORR in alkaline media [84] and that step sites and concave sites are the most active in acidic media [80,84]. Besides ORR, this technique revealed that the edges of single MoS_2 and $MoSe_2$ flakes are more active than basal planes for the hydrogen evolution reaction, but that the latter can be activated upon bombarding with He-ions [85].

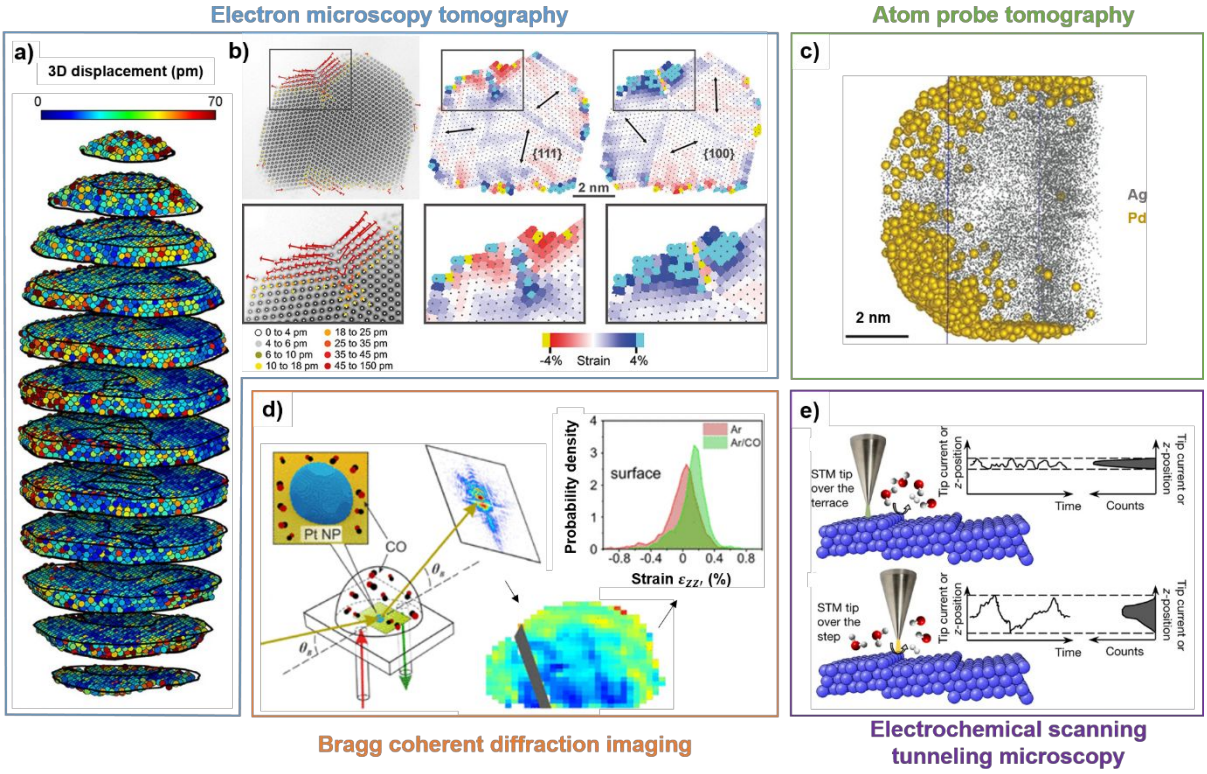

Figure 5. Determining the nature and structure of the catalytically active sites. (a) 3D atomic displacements measured in a FePt nanoparticle using GENFIRE algorithm from AC-STEM images; (b) Atomic resolution STEM images, with atomic displacement and strain maps within two crystallographic planes, as indicated in the Pt nanoparticle; (c) APT data showing the atom map from a Ag@Pd nanoparticle; (d) Sketch of the BCDI setup, 2D slice of the strain field through the center of a reconstructed Pt nanoparticle under Ar/CO flow and associated probability density of the strain field; (e) Scheme explaining the concept of using EC-STM noise analysis to reveal the catalytic sites under reaction conditions. Panel (a) is adapted with permission from Ref [22]. Copyright 2017 Springer Nature. Panel (b) is adapted with permission from Ref [21]. Copyright 2018 Springer Nature. Panel (c) is adapted with permission from Ref [63]. Copyright 2011 Springer Nature. Panel (d) is adapted with permission from Ref [68]. Copyright 2019 American Chemical Society. Panel (e) is adapted with permission from Ref [80]. Copyright 2017 Springer Nature.

CONCLUSION

In summary, the defect engineering approach has the particularity to touch the extreme complexity of nanoscale intrinsic structural disorder. Contrary to the 'classical'

surface science approach, the connection between theoretical computations (and their necessary simplifying assumptions) and experimental measurements on practical systems is not yet established. Numerous theoretical descriptors have nonetheless been applied to complex surfaces. For example, the generalized coordination number ($\overline{\mathrm{CN}}$) theory predicts the benefits of locally concave surface curvature, but without considering the local strain possibly generated by surface roughness. On the contrary, experimental observations (electron microscopy, X-ray diffraction) reveal significant local strain in the vicinity of structural defects. From this factual result, local strain alone (without considering the coordination effect) is a desirable experimental structural descriptor of surface defectiveness, able to rationalize the electrochemical adsorption behavior of disordered nanocatalysts, whereas each surface $\overline{\mathrm{CN}}$ remains hardly accessible in practice.

Consequently, there are currently no clear theoretical guidelines driving the 'defective-by-design' engineering of catalytic materials, and computational models must be adapted to better describe experimental observations (and not the other way around). Practical descriptors, however, suggest that maximizing surface distortion is an

efficient approach to boost catalytic performance, and the introduction of grain boundaries or surface dealloying were identified as experimental levers to implement such distortion. If practical structural descriptors inherit the limitations of their characterization technique(s) (resolution, artefacts, (un)realistic sample environment etc.), the constant technical development and fast progresses of instrumental tools predict an ongoing improvement of their descriptive power.

Finally, one could reasonably think that the ultimate goal in the defect engineering approach is to identify the structure of the most catalytically active site, and to maximize its implementation on nanocatalyst surface. This would be missing an important subtlety of this approach: the most active site is not necessarily desirable. It depends on the compromise between the resulting site activity and the number of (neighboring) sites that are ‘sacrificed’ to this purpose. This adds an extra layer of complexity above the previously mentioned. One thing certain, there is still a lot to uncover.

AUTHOR INFORMATION

Corresponding Authors

* E-mail for R.C.: raphael.chattot@grenoble-inp.org.

* E-mail for F.M.: frederic.maillard@lepmi.grenoble-inp.fr.

ORCID

R.C: 0000-0001-6169-530X

P.B: 0000-0002-1488-2257

I.M: 0000-0001-8342-6629

J.D: 0000-0002-9520-1555

L.D: 0000-0001-9520-1435

F.M: 0000-0002-2325-6645

Author contributions

All authors discussed the results and contributed to the final manuscript.

CONFLICT OF INTEREST

The authors declare no competing financial interest

ASSOCIATED CONTENT

Supporting Information.

The Supporting Information is available free of charge via the Internet at http://pubs.acs.org. It includes:

-Discussion on the extraction of the microstrain parameter from powder X-ray diffraction experiments with the Rietveld method

-Discussion on the correction of the as-measured microstrain to describe surface defectiveness.

-A plot bridging the specific activity for the ORR and the $Q_{CO}/2Q_{H}$ ratio

ACKNOWLEDGEMENTS

This work was performed within the framework of the Centre of Excellence of Multifunctional Architectured Materials 'CEMAM' (grant number ANR-10-LABX-44-

01). The authors acknowledge financial support from the French National Research Agency through the BRIDGE project (grant number ANR-19-ENER-0008-01).

REFERENCES

(1) Li, W.; Wang, D.; Zhang, Y.; Tao, L.; Wang, T.; Zou, Y.; Wang, Y.; Chen, R.; Wang, S. Defect Engineering for Fuel-Cell Electrocatalysts. *Adv. Mater.* **2020**, 1907879.

(2) Nørskov, J. K.; Bligaard, T.; Rossmeisl, J.; Christensen, C. H. Towards the Computational Design of Solid Catalysts. *Nat. Chem.* **2009**, *1* (1), 37–46.

(3) Zhao, Z.; Liu, S.; Zha, S.; Cheng, D.; Studt, F.; Henkelman, G.; Gong, J. Theory-Guided Design of Catalytic Materials Using Scaling Relationships and Reactivity Descriptors. *Nat. Rev. Mater.* **2019**, *4*, 792–804.

(4) Nørskov, J. K.; Rossmeisl, J.; Logadottir, a.; Lindqvist, L.; Kitchin, J. R.; Bligaard, T.; Jónsson, H. Origin of the Overpotential for Oxygen Reduction at a Fuel-Cell Cathode. *J. Phys. Chem. B* **2004**, *108* (46), 17886–17892.

(5) Robinson, P. J.; Holbrook, K. A. Why Gold Is the Noblest of All the Metals. *Nature* **1995**, *376* (July), 238–240.

(6) Hammer, B.; Nørskov, J. K. Electronic Factors Determining the Reactivity of Metal Surfaces. *Surf. Sci.* **1995**, *343* (3), 211–220.

(7) Batchelor, T. A. A.; Pedersen, J. K.; Winther, S. H.; Castelli, I. E.; Jacobsen, K. W.; Rossmeisl, J. High-Entropy Alloys as a Discovery Platform for Electrocatalysis. *Joule* **2019**, *3* (3), 834–845.

(8) Le Bacq, O.; Pasturel, A.; Chattot, R.; Previdello, B.; Nelayah, J.; Asset, T.; Dubau, L.; Maillard, F. Effect of Atomic Vacancies on the Structure and the Electrocatalytic Activity of Pt-Rich/C Nanoparticles: A Combined Experimental and Density Functional Theory Study. *ChemCatChem* **2017**, *9* (12), 2324–2338.

(9) Calle-Vallejo, F.; Tymoczko, J.; Colic, V.; Quang, H. V.; Pohl, M. D.; Morgenstern, K.; Loffreda, D.; Sautet, P.; Schuhmann, W.; Bandarenka, A. S. Finding Optimal Surface Sites on Heterogeneous Catalysts by Counting Nearest Neighbors. *Science* **2015**, *350* (6257), 185–190.

(10) Ma, X.; Xin, H. Orbitalwise Coordination Number for Predicting Adsorption

Properties of Metal Nanocatalysts. *Phys. Rev. Lett.* **2017**, *118* (January), 036101.

(11) Wu, D.; Dong, C.; Zhan, H.; Du, X. Bond-Energy-Integrated Descriptor for Oxygen Electrocatalysis of Transition Metal Oxides. *J. Phys. Chem. Lett.* **2018**, *9*, 3387–3391.

(12) Rietveld, H. M. A Profile Refinement Method for Nuclear and Magnetic Structures. *J. Appl. Crystallogr.* **1969**, *2* (2), 65–71.

(13) Chattot, R.; Bacq, O. Le; Beermann, V.; Kühl, S.; Herranz, J.; Henning, S.; Kühn, L.; Asset, T.; Guétaz, L.; Renou, G.; Drnec, J.; Bordet, P.; Pasturel, A.; Eychmüller, A.; Schmidt, T. J.; Strasser, P.; Dubau, L.; Maillard, F. Surface Distortion as a Unifying Concept and Descriptor in Oxygen Reduction Reaction Electrocatalysis. *Nat. Mater.* **2018**, *17* (9), 827–833.

(14) Billinge, S. J. L. The Rise of the X-Ray Atomic Pair Distribution Function Method: A Series of Fortunate Events. *Philos. Trans. R. Soc. A* **2019**, *377* (2147), 20180413.

(15) Thompson, P.; Cox, D. E.; Hastings, J. B. Rietveld Refinement of Debye–

Scherrer Synchrotron X-Ray Data from Al_2O_3. *J. Appl. Crystallogr.* **1987**, *20* (2), 79–83.

(16) Harada, M.; Ikegami, R.; Kumara, L. S. R.; Kohara, S.; Sakata, O. Reverse Monte Carlo Modeling for Local Structures of Noble Metal Nanoparticles Using High-Energy XRD and EXAFS. *RSC Adv.* **2019**, *9* (51), 29511–29521.

(17) Chattot, R.; Asset, T.; Bordet, P.; Drnec, J.; Dubau, L.; Maillard, F. Beyond Strain and Ligand Effects: Microstrain-Induced Enhancement of the Oxygen Reduction Reaction Kinetics on Various PtNi/C Nanostructures. *ACS Catal.* **2017**, *7*, 398–408.

(18) Sneed, B. T.; Young, A. P.; Tsung, C. K. Building up Strain in Colloidal Metal Nanoparticle Catalysts. *Nanoscale* **2015**, *7* (29), 12248–12265.

(19) Gan, L.; Yu, R.; Luo, J.; Cheng, Z.; Zhu, J. Lattice Strain Distributions in Individual Dealloyed Pt-Fe Catalyst Nanoparticles. *J. Phys. Chem. Lett.* **2012**, *3* (7), 934–938.

(20) Suzana, A. F.; Rochet, A.; Passos, A. R.; Castro Zerba, J. P.; Polo, C. C.; Santilli, C. V.; Pulcinelli, S. H.; Berenguer, F.; Harder, R.; Maxey, E.; Meneau,

F. *In Situ* Three-Dimensional Imaging of Strain in Gold Nanocrystals during Catalytic Oxidation. *Nanoscale Adv.* **2019**, *1* (8), 3009–3014.

(21) Nilsson Pingel, T.; Jørgensen, M.; Yankovich, A. B.; Grönbeck, H.; Olsson, E. Influence of Atomic Site-Specific Strain on Catalytic Activity of Supported Nanoparticles. *Nat. Commun.* **2018**, *9*, 2722.

(22) Yang, Y.; Chen, C. C.; Scott, M. C.; Ophus, C.; Xu, R.; Pryor, A.; Wu, L.; Sun, F.; Theis, W.; Zhou, J.; Eisenbach, M.; Kent, P. R. C.; Sabirianov, R. F.; Zeng, H.; Ercius, P.; Miao, J. Deciphering Chemical Order/Disorder and Material Properties at the Single-Atom Level. *Nature* **2017**, *542* (7639), 75–79.

(23) Ruiz-Zepeda, F.; Gatalo, M.; Pavlišič, A.; Dražić, G.; Jovanovič, P.; Bele, M.; Gaberščček, M.; Hodnik, N. Atomically Resolved Anisotropic Electrochemical Shaping of Nano-Electrocatalyst. *Nano Lett.* **2019**, *19* (8), 4919–4927.

(24) Stukowski, A.; Markmann, J.; Weissmüller, J.; Albe, K. Atomistic Origin of Microstrain Broadening in Diffraction Data of Nanocrystalline Solids. *Acta Mater.* **2009**, *57* (5), 1648–1654.

(25) Montejano-Carrizales, J. M.; Morán-López, J. L. Geometrical Characteristics of

Compact Nanoclusters. *Nanostructured Mater.* **1992**, *1* (5), 397–409.

(26) Chattot, R.; Martens, I.; Scohy, M.; Drnec, J.; Maillard, F.; Dubau, L. Disclosing Pt-Bimetallic Alloy Nanoparticle Surface Lattice Distortion with Electrochemical Probes. *ACS Energy Lett.* **2020**, *5* (1), 162–169.

(27) Henning, S.; Kühn, L.; Herranz, J.; Durst, J.; Binninger, T.; Nachtegaal, M.; Werheid, M.; Liu, W.; Adam, M.; Kaskel, S.; Eychmüller, A.; Schmidt, T. J. Pt-Ni Aerogels as Unsupported Electrocatalysts for the Oxygen Reduction Reaction. *J. Electrochem. Soc.* **2016**, *163* (9), F998–F1003.

(28) Henning, S.; Herranz, J.; Ishikawa, H.; Kim, B. J.; Abbott, D.; Kühn, L.; Eychmüller, A.; Schmidt, T. J. Durability of Unsupported Pt-Ni Aerogels in PEFC Cathodes. *J. Electrochem. Soc.* **2017**, *164* (12), F1136–F1141.

(29) Henning, S.; Ishikawa, H.; Kühn, L.; Herranz, J.; Müller, E.; Eychmüller, A.; Schmidt, T. J. Unsupported Pt-Ni Aerogels with Enhanced High Current Performance and Durability in Fuel Cell Cathodes. *Angew. Chemie - Int. Ed.* **2017**, *56* (36), 10707–10710.

(30) Li, M.; Zhao, Z.; Cheng, T.; Fortunelli, A.; Chen, C. Y.; Yu, R.; Zhang, Q.; Gu,

L.; Merinov, B. V.; Lin, Z.; Zhu, E.; Yu, T.; Jia, Q.; Guo, J.; Zhang, L.; Goddard, W. A.; Huang, Y.; Duan, X. Ultrafine Jagged Platinum Nanowires Enable Ultrahigh Mass Activity for the Oxygen Reduction Reaction. *Science* **2016**, *354* (6318), 1414–1419.

(31) Alia, S. M.; Ngo, C.; Shulda, S.; Ha, M. A.; Dameron, A. A.; Weker, J. N.; Neyerlin, K. C.; Kocha, S. S.; Pylypenko, S.; Pivovar, B. S. Exceptional Oxygen Reduction Reaction Activity and Durability of Platinum-Nickel Nanowires through Synthesis and Post-Treatment Optimization. *ACS Omega* **2017**, *2* (4), 1408–1418.

(32) Van Der Vliet, D. F.; Wang, C.; Tripkovic, D.; Strmcnik, D.; Zhang, X. F.; Debe, M. K.; Atanasoski, R. T.; Markovic, N. M.; Stamenkovic, V. R. Mesostructured Thin Films as Electrocatalysts with Tunable Composition and Surface Morphology. *Nat. Mater.* **2012**, *11* (12), 1051–1058.

(33) Bae, S. J.; Yoo, S. J.; Lim, Y.; Kim, S.; Lim, Y.; Choi, J.; Nahm, K. S.; Hwang, S. J.; Lim, T. H.; Kim, S. K.; Kim, P. Facile Preparation of Carbon-Supported PtNi Hollow Nanoparticles with High Electrochemical Performance. *J. Mater.*

Chem. **2012**, *22* (18), 8820–8825.

(34) Snyder, J.; Fujita, T.; Chen, M. W.; Erlebacher, J. Oxygen Reduction in Nanoporous Metal-Ionic Liquid Composite Electrocatalysts. *Nat. Mater.* **2010**, *9* (11), 904–907.

(35) Luo, M.; Sun, Y.; Zhang, X.; Qin, Y.; Li, M.; Li, Y.; Li, C.; Yang, Y.; Wang, L.; Gao, P.; Lu, G.; Guo, S. Stable High-Index Faceted Pt Skin on Zigzag-Like PtFe Nanowires Enhances Oxygen Reduction Catalysis. *Adv. Mater.* **2018**, *30* (10), 1705515.

(36) Dubau, L.; Nelayah, J.; Moldovan, S.; Ersen, O.; Bordet, P.; Drnec, J.; Asset, T.; Chattot, R.; Maillard, F. Defects Do Catalysis: CO Monolayer Oxidation and Oxygen Reduction Reaction on Hollow PtNi/C Nanoparticles. *ACS Catal.* **2016**, *6* (7), 4673–4684.

(37) Alia, S. M.; Pylypenko, S.; Neyerlin, K. C.; Kocha, S. S.; Pivovar, B. S. Nickel Nanowire Oxidation and Its Effect on Platinum Galvanic Displacement and Methanol Oxidation. *ECS Trans.* **2014**, *64* (3), 89–95.

(38) Xiong, Z.; Li, S.; Xu, H.; Zhang, K.; Yan, B.; Du, Y. Newly Designed Ternary

Metallic PtPdBi Hollow Catalyst with High Performance for Methanol and Ethanol Oxidation. *Catalysts* **2017**, *7*, 208.

(39) Mao, J.; Chen, W.; He, D.; Wan, J.; Pei, J.; Dong, J.; Wang, Y.; An, P.; Jin, Z.; Xing, W.; Tang, H.; Zhuang, Z.; Liang, X.; Huang, Y.; Zhou, G.; Wang, L.; Wang, D.; Li, Y. Design of Ultrathin Pt-Mo-Ni Nanowire Catalysts for Ethanol Electrooxidation. *Sci. Adv.* **2017**, *3*, e1603068.

(40) Zhao, S.; Li, M.; Han, M.; Xu, D.; Yang, J.; Lin, Y.; Shi, N. E.; Lu, Y.; Yang, R.; Liu, B.; Dai, Z.; Bao, J. Defect-Rich Ni_3FeN Nanocrystals Anchored on N-Doped Graphene for Enhanced Electrocatalytic Oxygen Evolution. *Adv. Funct. Mater.* **2017**, *28* (18), 1706018.

(41) Wang, P.; Jiang, K.; Wang, G.; Yao, J.; Huang, X. Phase and Interface Engineering of Platinum–Nickel Nanowires for Efficient Electrochemical Hydrogen Evolution. *Angew. Chemie - Int. Ed.* **2016**, *55* (41), 12859–12863.

(42) Dickens, C. F.; Nørskov, J. K. A Theoretical Investigation into the Role of Surface Defects for Oxygen Evolution on RuO_2. *J. Phys. Chem. C* **2017**, *121* (34), 18516–18524.

(43) Shi, Q.; Zhu, C.; Zhong, H.; Su, D.; Li, N.; Engelhard, M. H.; Xia, H.; Zhang, Q.; Feng, S.; Beckman, S. P.; Du, D.; Lin, Y. Nanovoid Incorporated Ir_xCu Metallic Aerogels for Oxygen Evolution Reaction Catalysis. *ACS Energy Lett.* **2018**, *3* (9), 2038–2044.

(44) Calle-Vallejo, F.; Pohl, M. D.; Bandarenka, A. S. Quantitative Coordination-Activity Relations for the Design of Enhanced Pt Catalysts for CO Electro-Oxidation. *ACS Catal.* **2017**, *7* (7), 4355–4359.

(45) Maillard, F.; Eikerling, M.; Cherstiouk, O. V; Schreier, S.; Savinova, E.; Stimming, U. Size Effects on Reactivity of Pt Nanoparticles in CO Monolayer Oxidation: The Role of Surface Mobility. *Faraday Discuss.* **2004**, *125*, 357–377.

(46) Van Der Vliet, D. F.; Wang, C.; Li, D.; Paulikas, A. P.; Greeley, J.; Rankin, R. B.; Strmcnik, D.; Tripkovic, D.; Markovic, N. M.; Stamenkovic, V. R. Unique Electrochemical Adsorption Properties of Pt-Skin Surfaces. *Angew. Chemie - Int. Ed.* **2012**, *51* (13), 3139–3142.

(47) Marichev, V. A. Reversibility of Platinum Voltammograms in Aqueous Electrolytes and Ionic Product of Water. *Electrochim. Acta* **2008**, *53* (27), 7952–

7960.

(48) Van Der Niet, M. J. T. C.; Garcia-Araez, N.; Hernández, J.; Feliu, J. M.; Koper, M. T. M. Water Dissociation on Well-Defined Platinum Surfaces: The Electrochemical Perspective. *Catal. Today* **2013**, *202*, 105–113.

(49) Janik, M. J.; McCrum, I. T.; Koper, M. T. M. On the Presence of Surface Bound Hydroxyl Species on Polycrystalline Pt Electrodes in the "Hydrogen Potential Region" (0 to 0.4 V-RHE). *J. Catal.* **2018**, *367*, 332–337.

(50) Tanaka, H.; Sugawara, S.; Shinohara, K.; Ueno, T.; Suzuki, S.; Hoshi, N.; Nakamura, M. Infrared Reflection Absorption Spectroscopy of OH Adsorption on the Low Index Planes of Pt. *Electrocatalysis* **2015**, *6* (3), 295–299.

(51) Garcia-Araez, N.; Climent, V.; Feliu, J. M. Analysis of Temperature Effects on Hydrogen and OH Adsorption on Pt(111), Pt(100) and Pt(110) by Means of Gibbs Thermodynamics. *J. Electroanal. Chem.* **2010**, *649* (1–2), 69–82.

(52) Zhang, C.; Firestein, K. L.; Fernando, J. F. S.; Siriwardena, D.; von Treifeldt, J. E.; Golberg, D. Recent Progress of *In Situ* Transmission Electron Microscopy for Energy Materials. *Adv. Mater.* **2019**, *32* (18), 1904094.

(53) Daio, T.; Staykov, A.; Guo, L.; Liu, J.; Tanaka, M.; Matthew Lyth, S.; Sasaki, K. Lattice Strain Mapping of Platinum Nanoparticles on Carbon and SnO_2 Supports. *Sci. Rep.* **2015**, *5*, 13126.

(54) Wang, Y.; Zhang, W. Mapping the Strain Distribution within Embedded Nanoparticles via Geometrical Phase Analysis. *Micron* **2019**, *125*, 102715.

(55) Ahmad, N.; Le Bouar, Y.; Ricolleau, C.; Alloyeau, D. Growth of Dendritic Nanostructures by Liquid-Cell Transmission Electron Microscopy: A Reflection of the Electron-Irradiation History. *Adv. Struct. Chem. Imaging* **2016**, *2*, 9.

(56) Kelly, T. F.; Miller, M. K. Atom Probe Tomography. *Rev. Sci. Instrum.* **2007**, *78*, 031101.

(57) Gault, B.; Breen, A. J.; Chang, Y.; He, J.; Jägle, E. A.; Kontis, P.; Kürnsteiner, P.; Kwiatkowski Da Silva, A.; Makineni, S. K.; Mouton, I.; Peng, Z.; Ponge, D.; Schwarz, T.; Stephenson, L. T.; Szczepaniak, A.; Zhao, H.; Raabe, D. Interfaces and Defect Composition at the Near-Atomic Scale through Atom Probe Tomography Investigations. *J. Mater. Res.* **2018**, *33* (23), 4018–4030.

(58) Li, T.; Bagot, P. A. J.; Marquis, E. A.; Tsang, S. C. E.; Smith, G. D. W.

Characterization of Oxidation and Reduction of Pt-Ru and Pt-Rh-Ru Alloys by Atom Probe Tomography and Comparison with Pt-Rh. *J. Phys. Chem. C* **2012**, *116* (33), 17633–17640.

(59) Li, T.; Kasian, O.; Cherevko, S.; Zhang, S.; Geiger, S.; Scheu, C.; Felfer, P.; Raabe, D.; Gault, B.; Mayrhofer, K. J. J. Atomic-Scale Insights into Surface Species of Electrocatalysts in Three Dimensions. *Nat. Catal.* **2018**, *1* (4), 300–305.

(60) Wilde, P.; Dieckhöfer, S.; Quast, T.; Xiang, W.; Bhatt, A.; Chen, Y. T.; Seisel, S.; Barwe, S.; Andronescu, C.; Li, T.; Schuhmann, W.; Masa, J. Insights into the Formation, Chemical Stability, and Activity of Transient Ni_yP@NiO_x Core-Shell Heterostructures for the Oxygen Evolution Reaction. *ACS Appl. Energy Mater.* **2020**, *3* (3), 2304–2309.

(61) Barroo, C.; Akey, A. J.; Bell, D. C. Atom Probe Tomography for Catalysis Applications: A Review. *Appl. Sci.* **2019**, *9* (13), 2721.

(62) Pfeiffer, B.; Erichsen, T.; Epler, E.; Volkert, C. A.; Trompenaars, P.; Nowak, C. Characterization of Nanoporous Materials with Atom Probe Tomography.

Microsc. Microanal. **2015**, *21* (3), 557–563.

(63) Tedsree, K.; Li, T.; Jones, S.; Chan, C. W. A.; Yu, K. M. K.; Bagot, P. A. J.; Marquis, E. A.; Smith, G. D. W.; Tsang, S. C. E. Hydrogen Production from Formic Acid Decomposition at Room Temperature Using a Ag-Pd Core-Shell Nanocatalyst. *Nat. Nanotechnol.* **2011**, *6* (5), 302–307.

(64) Abbey, B. From Grain Boundaries to Single Defects: A Review of Coherent Methods for Materials Imaging in the X-Ray Sciences. *Jom* **2013**, *65* (9), 1183–1201.

(65) Ulvestad, A.; Tripathi, A.; Hruszkewycz, S. O.; Cha, W.; Wild, S. M.; Stephenson, G. B.; Fuoss, P. H. Coherent Diffractive Imaging of Time-Evolving Samples with Improved Temporal Resolution. *Phys. Rev. B* **2016**, *93* (18), 184105.

(66) Carnis, J.; Gao, L.; Labat, S.; Kim, Y. Y.; Hofmann, J. P.; Leake, S. J.; Schülli, T. U.; Hensen, E. J. M.; Thomas, O.; Richard, M.-I. Towards a Quantitative Determination of Strain in Bragg Coherent X-Ray Diffraction Imaging: Artefacts and Sign Convention in Reconstructions. *Sci. Rep.* **2019**, *9*, 17357.

(67) Ulvestad, U.; Singer, A.; Clark, J. N.; Cho, H. M.; Kim, J. W.; Harder, R.; Maser, J.; Meng, Y. S.; Shpyrko, O. G. Topological Defect Dynamics in *Operando* Battery Nanoparticles. *Science* **2015**, *348* (6241), 1344–1347.

(68) Abuin, M.; Kim, Y. Y.; Runge, H.; Kulkarni, S.; Maier, S.; Dzhigaev, D.; Lazarev, S.; Gelisio, L.; Seitz, C.; Richard, M.-I.; Zhou, T.; Vonk, V.; Keller, T. F.; Vartanyants, I. A.; Stierle, A. Coherent X-Ray Imaging of CO-Adsorption-Induced Structural Changes in Pt Nanoparticles: Implications for Catalysis. *ACS Appl. Nano Mater.* **2019**, *2* (8), 4818–4824.

(69) Kim, D.; Chung, M.; Kim, S.; Yun, K.; Cha, W.; Harder, R.; Kim, H. Defect Dynamics at a Single Pt Nanoparticle during Catalytic Oxidation. *Nano Lett.* **2019**, *19* (8), 5044–5052.

(70) Sun, Y.; Liang, Y.; Luo, M.; Lv, F.; Qin, Y.; Wang, L.; Xu, C.; Fu, E.; Guo, S. Defects and Interfaces on PtPb Nanoplates Boost Fuel Cell Electrocatalysis. *Small* **2018**, *14* (3), 1702259.

(71) Fichtner, J.; Watzele, S.; Garlyyev, B.; Kluge, R. M.; Haimerl, F.; El-Sayed, H. A.; Li, W. J.; Maillard, F. M.; Dubau, L.; Chattot, R.; Michalička, J.; MacAk, J. M.;

Wang, W.; Wang, D.; Gigl, T.; Hugenschmidt, C.; Bandarenka, A. S. Tailoring the Oxygen Reduction Activity of Pt Nanoparticles through Surface Defects: A Simple Top-Down Approach. *ACS Catal.* **2020**, *10* (5), 3131–3142.

(72) Dou, S.; Tao, L.; Wang, R.; El Hankari, S.; Chen, R.; Wang, S. Plasma-Assisted Synthesis and Surface Modification of Electrode Materials for Renewable Energy. *Adv. Mater.* **2018**, *30* (21), 1705850.

(73) Ruge, M.; Drnec, J.; Rahn, B.; Reikowski, F.; Harrington, D. A.; Carlà, F.; Felici, R.; Stettner, J.; Magnussen, O. M. Structural Reorganization of Pt(111) Electrodes by Electrochemical Oxidation and Reduction. *J. Am. Chem. Soc.* **2017**, *139* (12), 4532–4539.

(74) Jacobse, L.; Huang, Y. F.; Koper, M. T. M.; Rost, M. J. Correlation of Surface Site Formation to Nanoisland Growth in the Electrochemical Roughening of Pt(111). *Nat. Mater.* **2018**, *17* (3), 277–282.

(75) Jacobse, L.; Rost, M. J.; Koper, M. T. M. Atomic-Scale Identification of the Electrochemical Roughening of Platinum. *ACS Cent. Sci.* **2019**, *5* (12), 1920–1928.

(76) Livet, F.; Beutier, G.; De Boissieu, M.; Ravy, S.; Picca, F.; Le Bolloc'H, D.; Jacques, V. Coherent Scattering from Silicon Monocrystal Surface. *Surf. Sci.* **2011**, *605*, 390–395.

(77) Nicolas, J. D.; Reusch, T.; Osterhoff, M.; Sprung, M.; Schülein, F. J. R.; Krenner, H. J.; Wixforth, A.; Salditt, T. Time-Resolved Coherent X-Ray Diffraction Imaging of Surface Acoustic Waves. *J. Appl. Crystallogr.* **2014**, *47* (5), 1596–1605.

(78) Kutsal, M.; Bernard, P.; Berruyer, G.; Cook, P. K.; Hino, R. The ESRF Dark-Field x-Ray Microscope at ID06. *IOP Conf. Ser. Mater. Sci. Eng.* **2019**, *580*, 012007.

(79) Morgan, A. J.; Prasciolu, M.; Andrejczuk, A.; Krzywinski, J.; Meents, A.; Pennicard, D.; Graafsma, H.; Barty, A.; Bean, R. J.; Barthelmess, M.; Oberthuer, D.; Yefanov, O.; Aquila, A.; Chapman, H. N.; Bajt, S. High Numerical Aperture Multilayer Laue Lenses. *Sci. Rep.* **2015**, *5*, 9892.

(80) Pfisterer, J. H. K.; Liang, Y.; Schneider, O.; Bandarenka, A. S. Direct Instrumental Identification of Catalytically Active Surface Sites. *Nature* **2017**, *549* (7670), 74–77.

(81) Sumetskii, M.; Kornyshev, A. A.; Stimming, U. Adatom Diffusion Characteristics from STM Noise: Theory. *Surf. Sci.* **1994**, *307–309*, 23–27.

(82) Sumetskii, M.; Kornyshev, A. A. Noise in STM Due to Atoms Moving in the Tunneling Space. *Phys. Rev. B* **1993**, *48* (23), 17493–17506.

(83) Hugelmann, M.; Schindler, W. Tunnel Barrier Height Oscillations at the Solid/Liquid Interface. *Surf. Sci.* **2003**, *541*, L643–L648.

(84) Liang, Y.; McLaughlin, D.; Csoklich, C.; Schneider, O.; Bandarenka, A. S. The Nature of Active Centers Catalyzing Oxygen Electro-Reduction at Platinum Surfaces in Alkaline Media. *Energy Environ. Sci.* **2019**, *12* (1), 351–357.

(85) Mitterreiter, E.; Liang, Y.; Golibrzuch, M.; McLaughlin, D.; Csoklich, C.; Bartl, J. D.; Holleitner, A.; Wurstbauer, U.; Bandarenka, A. S. *In-Situ* Visualization of Hydrogen Evolution Sites on Helium Ion Treated Molybdenum Dichalcogenides under Reaction Conditions. *npj 2D Mater. Appl.* **2019**, *3* (25).

FOR TABLE OF CONTENTS ONLY

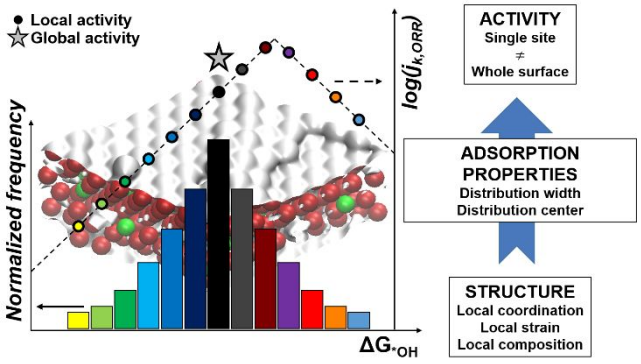

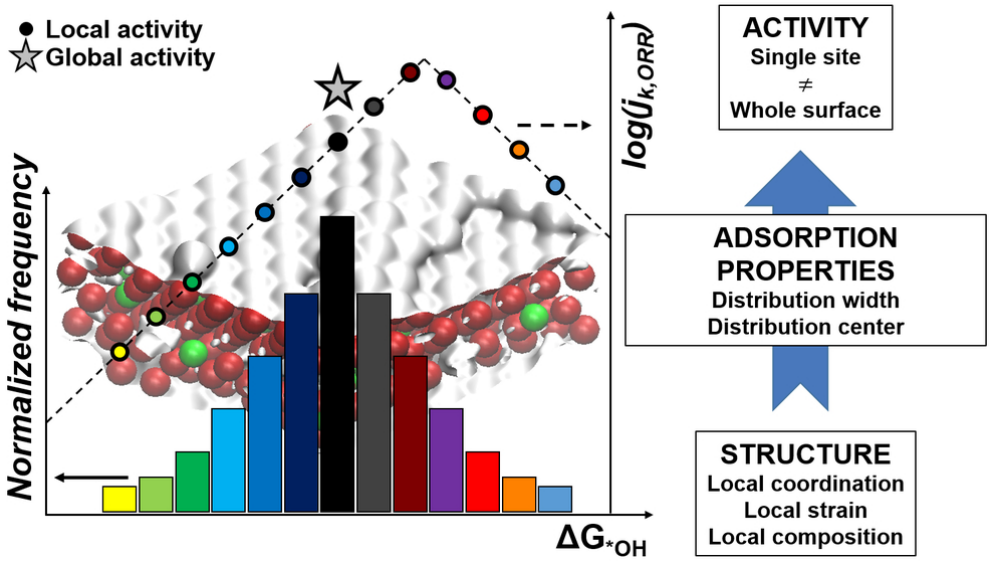

Every Piece Matters: Describing and quantifying surface structural disorder is essential for rationalizing the catalytic performance of defect-engineered nanocatalysts.

84x47mm (300 x 300 DPI)